

## Drag reduction utilizing a wall-attached ferrofluid film in turbulent channel flow

Neamtu-Halic, Marius M.; Holzner, Markus; Stancanelli, Laura M.

**DOI**

[10.1017/jfm.2024.735](https://doi.org/10.1017/jfm.2024.735)

**Publication date**

2024

**Document Version**

Final published version

**Published in**

Journal of Fluid Mechanics

**Citation (APA)**

Neamtu-Halic, M. M., Holzner, M., & Stancanelli, L. M. (2024). Drag reduction utilizing a wall-attached ferrofluid film in turbulent channel flow. *Journal of Fluid Mechanics*, 996, Article A35.  
<https://doi.org/10.1017/jfm.2024.735>

**Important note**

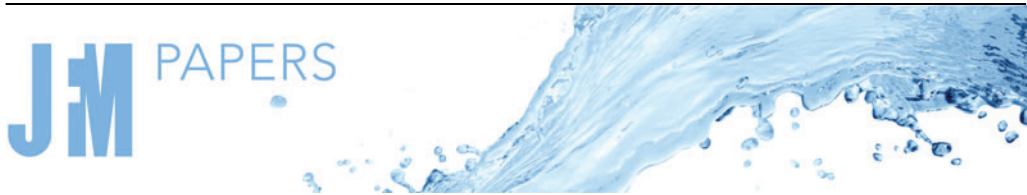
To cite this publication, please use the final published version (if applicable).  
Please check the document version above.

**Copyright**

Other than for strictly personal use, it is not permitted to download, forward or distribute the text or part of it, without the consent of the author(s) and/or copyright holder(s), unless the work is under an open content license such as Creative Commons.

**Takedown policy**

Please contact us and provide details if you believe this document breaches copyrights.  
We will remove access to the work immediately and investigate your claim.



# Drag reduction utilizing a wall-attached ferrofluid film in turbulent channel flow

Marius M. Neamtu-Halic<sup>1,2,4,†</sup>, Markus Holzner<sup>1,3,4</sup> and Laura M. Stancanelli<sup>5,6</sup>

<sup>1</sup>Swiss Federal Institute of Forest, Snow and Landscape Research WSL, 8903 Birmensdorf, Switzerland

<sup>2</sup>Institute of Environmental Engineering, ETH Zürich, 8039 Zürich, Switzerland

<sup>3</sup>Swiss Federal Institute of Aquatic Science and Technology Eawag, 8600 Dübendorf, Switzerland

<sup>4</sup>Institute of Hydraulic Engineering and River Research, University of Natural Resources and Life Sciences, BOKU Wien, 1190 Vienna, Austria

<sup>5</sup>Department of Hydraulic Engineering, Delft University of Technology, TU Delft, 2628CN Delft, The Netherlands

<sup>6</sup>Department of Civil, Environmental and Architectural Engineering, University of Padua, 35131 Padua, Italy

(Received 18 January 2024; revised 5 August 2024; accepted 5 August 2024)

This study explores the application of a wall-attached ferrofluid film to decrease skin-friction drag in turbulent channel flow. We conduct experiments using water as a working fluid in a turbulent channel flow set-up, where one wall is coated with a ferrofluid layer held in place by external permanent magnets. Depending on the flow conditions, the interface between the two fluids is observed to form unstable travelling waves. While ferrofluid coating has been previously employed in laminar and moderately turbulent flows (Reynolds number  $Re < 4000$ ) to reduce drag by creating a slip condition at the fluid interface, its effectiveness in fully developed turbulent conditions, particularly when the interface exhibits instability, remains uncertain. Our primary objective is to assess the effectiveness of ferrofluid coating in reducing turbulent drag with particular focus on scenarios when the ferrofluid layer forms unstable waves. To achieve this, we measure flow velocity using two-dimensional particle tracking velocimetry (2D-PTV), and the interface contour between the fluids is determined using an interface tracking algorithm. Our results reveal the significant potential of ferrofluid coating for drag reduction, even in scenarios where the interface between the surrounding fluid and ferrofluid exhibits instability, with observed drag reduction rates up to 95 %. In particular, waves with an amplitude significantly smaller than a viscous length scale positively contribute to drag reduction, while larger waves are detrimental, because of induced turbulent fluctuations.

† Email address for correspondence: [nemarius@ethz.ch](mailto:nemarius@ethz.ch)

However, for the latter case, slip outcompetes the extra turbulence so that drag is still reduced.

**Key words:** drag reduction, coating, magnetic fluids

---

## 1. Introduction

Over the last decades, a considerable research effort has been dedicated to the reduction of drag in turbulent flows. This interest stems primarily from the goal of decreasing energy consumption in various applications, such as fluid transportation through pipes or the movement of a vessel through a fluid.

Drag-reduction techniques are commonly classified into passive and active, the latter requiring external energy to be fed into the system (Gad-el Hak 1996; Quadrio & Ricco 2004).

Passive drag-reduction techniques can be classified into two categories: additives, primarily polymers mixed into the fluid, and surface property modification techniques. While the former are employed in the turbulent regime only, the latter are especially efficient in laminar flows. Additives are used to reduce turbulence intensity or alter the apparent viscosity of the fluid (Lumley 1969; White & Mungal 2008; Zhang, Duan & Muzychka 2021). Virk's influential work in the 1970s demonstrated that the drag reduction achieved with polymer additives asymptotically approaches a maximum value (Virk, Mickley & Smith 1970), the so-called Virk asymptote. On the other hand, surface property modification techniques focus on altering the characteristics of the wall. A typical example is the creation of micro- and nano-textures that trap microscopic gas pockets, resulting in the Cassie–Baxter state, which is a superhydrophobic surface (Liravi *et al.* 2020). Recently, it has been demonstrated that these surfaces might also be effective to reduce flow separation, and thus form drag, over a bluff body in a turbulent channel flow (Mollicone *et al.* 2022). Other examples include the use of microscale protuberances (Dean & Bhushan 2010; Saranadhi *et al.* 2016; Costantini, Mollicone & Battista 2018) and the application of chemical surface coatings (Solomon, Khalil & Varanasi 2014; Kim *et al.* 2020).

Initial observations of natural surfaces in contact with fluids, such as shark skin, prompted scientists to investigate the impact of surface texture on drag reduction. They discovered that regular riblets on solid surfaces can hinder the formation of coherent flow structures near the surface (Choi, Moin & Kim 1993). These vortical flow structures promote the transfer of momentum perpendicular to the surface, and their suppression dampened this transfer and hence drag (Kim & Hussain 1993; Dean & Bhushan 2010). Building upon these findings, recent active techniques have emerged that utilize cyclic wall movements perpendicular to the flow direction to control the formation of vortical structures near solid surfaces, aiming to reduce drag (Quadrio & Ricco 2004; Quadrio, Ricco & Viotti 2009; Ricco, Skote & Leschziner 2021). Remarkably, drag reduction of up to 45 % was achieved under optimal conditions, although the energy balance between the power saved through oscillation and the power expended to activate the wall motions was typically limited to 7 % at the most. Another established technique involves creating streamwise travelling waves of wall deformation. Depending on the maximum wall displacement and wave periods, this technique can result in either drag reduction or an increase in drag (Nakanishi, Mamori & Fukagata 2012; Nabae, Kawai & Fukagata 2020). For a comprehensive review of this method, we refer to the recent work by Fukagata, Iwamoto & Hasegawa (2024).

Recent investigations have delved into harnessing magnetically controllable fluids, particularly ferrofluids, to form a slim coating on the wall effectively establishing a slip boundary condition. Although this passive technique was initially developed for microfluidic devices (Dev *et al.* 2022), its feasibility in macroscopic flows has recently been demonstrated by Stancanelli, Secchi & Holzner (2024) in laminar and moderately turbulent regimes. However, it is known that the ferrofluid interface can be subject to instability giving rise to travelling waves at high flow velocities, posing the question about their effectiveness at higher Reynolds numbers (Kögel, Völkel & Richter 2020; Völkel, Kögel & Richter 2020).

The aim of this work is to reveal the drag-reduction efficiency of a ferrofluid coating when instabilities at the interface occur in the turbulent regime. Our goal is to systematically explore various turbulent flow regimes and magnetic field strengths to establish connections between interface wave characteristics and drag reduction. While distinct from the study conducted by Dev *et al.* (2022), which focused on microfluidic laminar scenarios, our research builds on that of Stancanelli *et al.* (2024) by incorporating the instability of ferrofluid interfaces and covering higher Reynolds numbers.

The structure of this paper is outlined as follows. Section 2 provides a detailed description of the methodology employed. Section 3 presents the findings obtained from the study. Finally, the paper concludes with a summary and the main conclusions in § 4.

## 2. Methods

### 2.1. Experimental set-up

In this work, experiments were conducted using a Plexiglas® channel, with a square cross-section of dimensions  $25 \times 25 \text{ mm}^2$  and 1000 mm in length.

A layer of ferrofluid was introduced at the top of the channel at a distance of 500 mm from the conduit inlet. The ferrofluid layer had a length of approximately 300 mm and a height of approximately 3 mm. To hold the ferrofluid in place, 14 stacks of 9 magnets (each with dimensions  $3 \times 3 \times 20 \text{ mm}^3$  Neodymium 45 from Supermagnete) were positioned at gap intervals of 2 mm in the  $x$  (streamwise) direction covering the entire length of the ferrofluid layer. The arrangement is depicted schematically in figure 1. To create the layer, the ferrofluid was introduced with a syringe at an injection point located in the proximity of the magnetic array. As a result of the magnetic attractive force, the ferrofluid spread evenly across the entire wall section covered by the magnetic array.

The magnetic field generated by the magnets was tangentially oriented to the ferrofluid layer in the  $z$  spanwise direction. The intensity of the magnetic field, denoted as  $H$ , was measured using a PCE-MFM 4000 gaussmeter. Figure 1 illustrates the tangential magnetic field intensity as a function of the distance from the magnets. As observed, the magnetic field exhibits an exponential decrease with distance  $y$  in the vertical direction. Throughout this study, we varied the magnetic field intensity by adjusting the position of the magnet array relative to the top wall of the channel.

A closed-loop circulation of water through the channel was realized with the following specifications. Water was pumped out of a reservoir using a water pump (LIVERANI model EP-MINI 3/4) and directed to a water tower with a fixed pressure head. From there, the water was directed through the Plexiglas® channel and returned to the reservoir. Control over flow discharge and pressure inside the channel was achieved using two valves positioned upstream and downstream of the Plexiglas® channel, respectively. The flow rate was measured by a flow meter (SIEMENS model SITRANS FM MAG 1100) installed at the inlet of the channel.

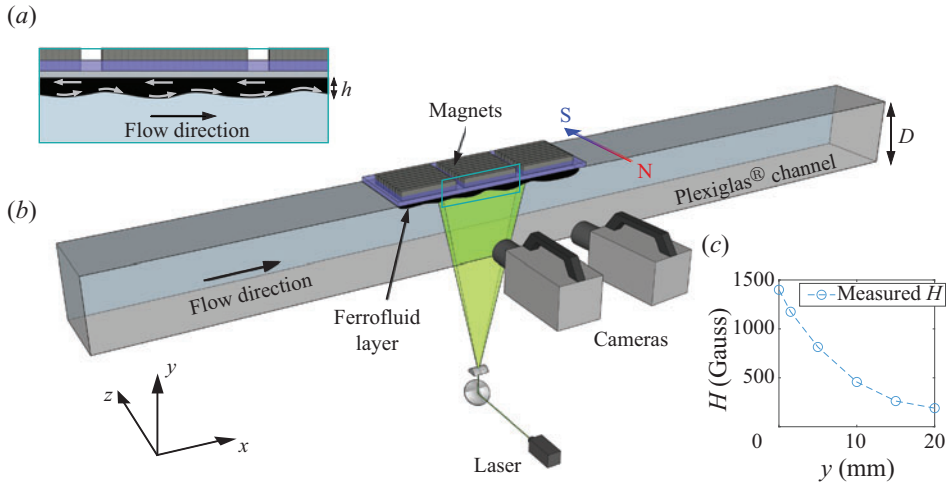


Figure 1. Sketch of the set-up (b). Detail of the ferrofluid layer showing schematically the ferrofluid recirculation (a). Measured spanwise magnetic field intensity  $H$  as a function of distance  $y$  from the permanent magnets (c).

High-speed imaging was used to characterize the ferrofluid interface and the flow at a distance of 200 mm away from the ferrofluid leading edge, where the interface waves and the flow reached an equilibrium, i.e. conditions are homogeneous in the streamwise direction. Flow measurements were performed using two-dimensional particle tracking velocimetry (2D-PTV) in a vertical plane aligned with the flow direction and passing through the centre of the channel (figure 1), where the flow is statistically 2-D. For this purpose, the flow was seeded with neutrally buoyant polystyrene particles with a diameter of 11  $\mu\text{m}$ . To visualize the particles, a laser sheet was generated using a solid state 532 nm green laser (CNI Laser model MGL-FN-532). A high-speed camera (Photron model SA5), operating at a frequency of 4000 Hz, was employed to capture the movement of the particles within an observation window of approximately  $25 \times 25 \text{ mm}^2$ . In our measurements, we estimate relative errors of 5 % for velocity measurements and 12 % for shear stresses (Stancanelli *et al.* 2024).

To analyse the motion of the interface, a second high-speed camera (operating at frequency in the range of 1000–3000 Hz) was employed, which covered a larger observation volume of approximately  $60 \times 25 \text{ mm}^2$ . To identify and extract the interface, a median filter with a kernel size of approximately 11 pixels was first applied. Then the interface was detected using a threshold on the grey value intensity. Based on this method, the local interface height is estimated with a relative error of 1 %. Exemplary videos showing the motion of the interface are provided in the supplementary movies available at <https://doi.org/10.1017/jfm.2024.735>.

## 2.2. Experiments

A total of 18 experiments were carried out, at four different magnetic field intensities  $H$  in the range 140–460 Gs (see table 1). For each magnetic field intensity, five different flow rates were used varying the Reynolds numbers  $Re = U(D - h)/\nu$  in the range 2500–12 500, where  $U$  is the space and time average streamwise flow velocity,  $\nu$  is the water kinematic viscosity,  $D$  the channel height and  $h$  the ferrofluid layer height (figure 1).

Label	$Re$	$H$ (Gs)	$h$ (mm)	$U$ (m s <sup>-1</sup> )	Symbol
a.1	2740	460	2.95	0.11	●
a.2	5080	460	3.04	0.20	●
a.3	7430	460	3.04	0.30	●
a.4	9850	460	3.09	0.40	●
a.5	12 380	460	3.11	0.50	●
b.1	2580	250	3.13	0.10	●
b.2	5030	250	3.20	0.20	●
b.3	7200	250	3.25	0.30	●
b.4	9820	250	3.28	0.40	●
b.5	12 230	250	3.38	0.50	●
c.1	2780	170	2.87	0.10	●
c.2	5270	170	3.14	0.21	●
c.3	7740	170	3.12	0.31	●
c.4	10 150	170	3.10	0.40	●
c.5	12 660	170	2.82	0.50	●
d.1	3090	140	3.21	0.12	●
d.2	5100	140	2.88	0.21	●
d.3	7300	140	3.23	0.30	●

Table 1. Overview of the experimental parameters, where  $Re$  is the Reynolds number,  $H$  the magnetic field intensity,  $h$  the time-space average height of the ferrofluid layer,  $U$  the time-space average streamwise velocity of ambient fluid. Letters ranging from ‘a’ to ‘d’ on the label represent the magnetic field intensity ( $H$ ), while the numbers correspond to the Reynolds number. The colour-code depicts the magnetic field intensity while the bullet size varies with  $Re$  number.

During these experiments, no detachment of ferrofluid was observed. Conversely, for the lower magnetic field intensity  $H = 140$  Gs, only three experiments were conducted as the ferrofluid layer was subject to detachment at the two highest Reynolds-number cases. The experimental parameters are reported in [table 1](#).

3. Results and discussion

3.1. Stability of the ferrofluid interface

As a first step in our analysis, we scrutinize the behaviour of the wall coating, with a focus on the dynamics of the interface between ferrofluid and water. In [figure 2](#), we show a snapshot of the interface at different Reynolds numbers and fixed magnetic field intensity ( $H = 170$  Gs). When the Reynolds number is low ([figure 2a](#)), the interface appears rather flat. However, as the Reynolds number is raised, we observe the emergence of an interfacial instability, manifested in the form of travelling waves. These waves resemble those arising from a shear (i.e. Kelvin–Helmholtz) instability (Kögel *et al.* 2020; Völkel *et al.* 2020).

To characterize the waves, we conduct an image postprocessing analysis as follows. The interface height is denoted as  $h(x, t)$ , where  $x$  represents the streamwise coordinate and  $t$  denotes the time. The interface elevation relative to its mean is  $\zeta(x, t) = h(x, t) - \overline{h(x)}$ , where  $\overline{h(x)}$  is the time-averaged height of the interface. To characterize the unstable waves, we identify the zero upcrossings of the time signal  $\zeta(x_0, t)$  at various locations  $x = x_0$  (10 points along the horizontal coordinate with equal spacing of  $\approx 5.5$  mm). We then calculate the average wave amplitude,  $a$ , defined as the difference between the maximum and minimum of  $\zeta(x_0, t)$  between two adjacent zero upcrossings, and then average this value over all events and  $x_0$  locations. Similarly, the wave period  $T$  is computed as the average time span between zero upcrossings, and the wave frequency  $\omega$  is defined as  $\omega = 1/T$ .

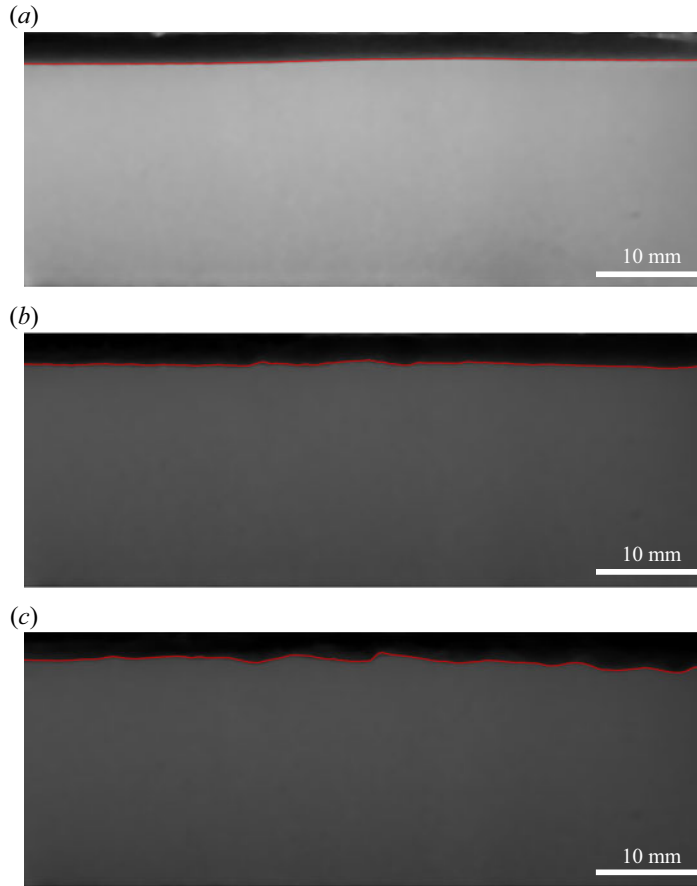


Figure 2. Instantaneous snapshot of the ferrofluid interface at  $H = 170$  Gs for  $Re = 2780$ , cf. experiment c.1 (a),  $Re = 7740$ , c.3 (b) and  $Re = 12660$ , c.5 (c).

Finally, to calculate the average wavelength  $L$ , we calculate the distance between the zero upcrossings of the spatial signal  $\zeta(x, t_0)$  at fixed times  $t_0$  and average this measurement over all instances.

A synthesis of average wave characteristics across all experiments is outlined in [table 2](#).

To contextualize the relative influence of the governing parameters, i.e. average water flow velocity  $U$  and magnetic field intensity, we employ linear stability analysis. To this end, we compute the critical velocity curves, denoted as  $U_{crit}$ , which represent the average water velocity threshold for the onset of unstable travelling waves. These critical velocity curves are determined as a function of the magnetic field intensity  $H$  and the wavenumber  $k$  (Kögel *et al.* 2020; Völkel *et al.* 2020), defined as

$$U_{crit}(k, H) = \sqrt{\frac{\rho_f + \rho_w}{\rho_f \rho_w} \left( k\gamma + \tilde{\mu}H^2 + \frac{g(\rho_f - \rho_w)}{k} \right)}, \quad (3.1)$$

where  $\rho_f$  is the ferrofluid density,  $\rho_w$  is the ambient fluid density,  $\gamma$  is the interface tension between the two fluids and  $\tilde{\mu} = \mu_0 \chi^2 / (\chi + 2)$  is proportional to the vacuum permeability  $\mu_0$  and depends on the susceptibility  $\chi$  (the ferrofluid properties are given in [table 3](#)). [Figure 3](#) displays the critical velocity neutral curves for our experiments, along with



Label	$a$ (mm)	$L$ (mm)	$\omega$ (s <sup>-1</sup> )	Symbol	Stability
a.1	0.02	1.40	82.6	●	stable
a.2	0.04	1.64	83.1	●	stable
a.3	0.02	2.45	52.5	●	stable
a.4	0.03	2.00	106.1	●	stable
a.5	0.10	2.47	103.1	●	unstable
b.1	0.02	1.57	92.3	●	stable
b.2	0.02	1.66	77.4	●	stable
b.3	0.03	1.72	119.8	●	unstable
b.4	0.18	2.62	87.7	●	unstable
b.5	0.16	3.91	68.7	●	unstable
c.1	0.02	1.53	58.2	●	stable
c.2	0.02	1.94	88.9	●	unstable
c.3	0.13	4.93	35.1	●	unstable
c.4	0.46	6.28	30.1	●	unstable
c.5	0.33	6.57	34.4	●	unstable
d.1	0.07	1.70	65.4	●	stable
d.2	0.04	2.01	100.9	●	unstable
d.3	0.42	7.11	26.3	●	unstable

Table 2. Overview of wave characteristics, where  $a$  is the wave amplitude,  $L$  the wavelength and  $\omega$  the wave time frequency. Letters ranging from ‘a’ to ‘d’ on the label represent the magnetic field intensity ( $H$ ), while the numbers correspond to the Reynolds number. The colour-code depicts the magnetic field intensity while the symbol size varies with  $Re$  number.

Property	Value
density $\rho_f$ (kg m <sup>-3</sup> )	1210
viscosity $\mu_f$ (cSt)	6
magnetic susceptibility $\chi$ (T (A m <sup>-1</sup> ) <sup>-1</sup> )	0.32
surface tension $\gamma$ (mN m <sup>-1</sup> )	43

Table 3. Properties of ferrofluid EFH1 (from Ferrotec USA corporate).

the measured values of  $U$  (the bulk average flow velocity) and  $k = 2\pi/L$  (the average wavenumber of the interface). The neutral curves separate stable (below) from unstable (above) behaviour. The increase in the intensity of the magnetic field  $H$  is a stabilizing factor for the ferrofluid interface (shifting the neutral curve upwards). Conversely, an increase in the average flow velocity of the ambient fluid is destabilizing. Experiments with a given magnetic field intensity show that as  $Re$  (represented by colour-matched dots, ranging from larger to smaller) increases, there is a decrease in wavenumber ( $k$ ). Remarkably, when the magnetic field is at its strongest,  $H = 460$  Gs, only one flow case exhibits instability ( $Re = 12\,380$ , i.e. experiment a.5 in table 1). However, with a magnetic field intensity of  $H = 170$  Gs, nearly all flow cases exhibit instability, except for one experiment (experiment c.1 in table 1 corresponding to  $Re = 2780$ ). This is qualitatively consistent with figure 2 where the interface is rather smooth for c.1, whereas for c.3 and c.5 it is corrugated.

To statistically characterize the wave frequency spectra, we conduct a Fourier analysis of the interface elevation. This involves computing the temporal power spectral density of the interface elevation,  $\zeta(x, t)$ . The power spectra are then averaged over all locations to obtain a single average temporal power spectrum density for each experiment.



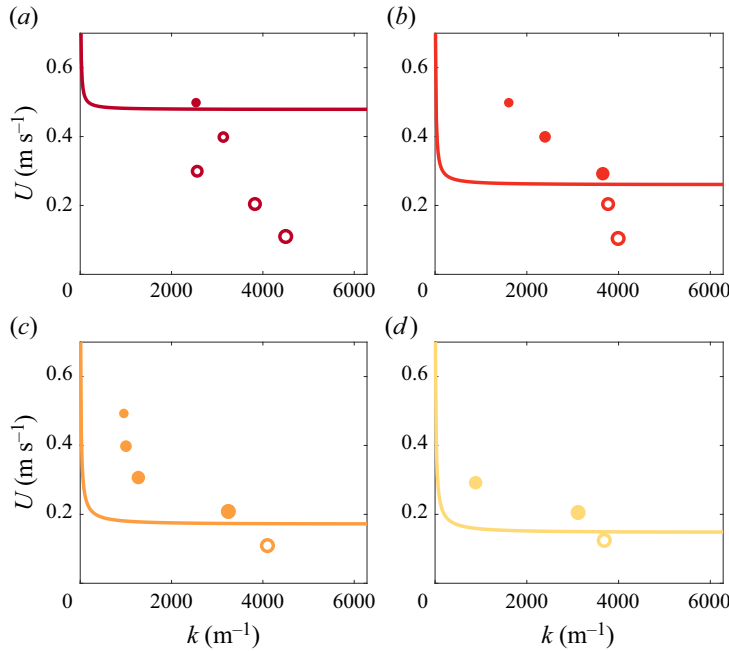


Figure 3. Stability maps for the experiments with  $H = 460$  Gs (a),  $H = 250$  Gs (b),  $H = 170$  Gs (c) and  $H = 140$  Gs (d). The colour-coding and bullet size are as specified in table 1. Empty symbols denote experiments featuring a stable interface, while filled symbols indicate cases characterized by an unstable interface.

The power spectrum computation utilizes Welch's method through the 'pwhelch' function in MATLAB.

Figure 4 displays the temporal power spectrum density of the interface elevation for the experiments detailed in table 1. In this figure, the Reynolds number increases from left to right, while the magnetic field intensity ( $H$ ) rises from the bottom to the top. Focusing on the first column (a.1–d.1), which pertains to experiments with the lowest Reynolds numbers, we observe that the spectra exhibit maxima near the origin of the abscissa, followed by a rapid decay as the frequency ( $f$ ) increases. This suggests that the interface remains mostly flat in these experiments.

Let us now consider the scenario with  $H = 460$  Gs (figure 4 a.1–a.5). As the Reynolds number increases, the power spectra begin to fill the range of 0–100 Hz, with no distinct peak. That is, a range of waves starts to emerge without a dominant frequency. As the magnetic field decreases, a clear peak becomes evident in the power spectra at higher Reynolds numbers (as seen in, for instance, b.5, c.5, d.3). The prominence of this peak intensifies as the flow cases move upward from the corresponding instability curves depicted in figure 3. The presence of a distinct peak suggests the occurrence of monochromatic cylindrical waves at the interface (refer to cases c.4, c.5, d.3). In instances of multiple frequencies, the interface is characterized by a train of waves exhibiting different harmonics (see case a.5), indicating irregular wave patterns. Finally, increasing the magnetic field leads to a higher frequency manifestation of instability ( $H$  acting as a stabilizing factor), indicated by a rightward shift in the peak (observe cases c.5 and b.5).

To characterize the spatio-temporal wave dynamics, in figure 5 we present space–time diagrams of the interface elevation  $\zeta$ . Observing figure 5, it is noticeable that the interface displays a relatively flat profile when the Reynolds numbers are low and the magnetic field

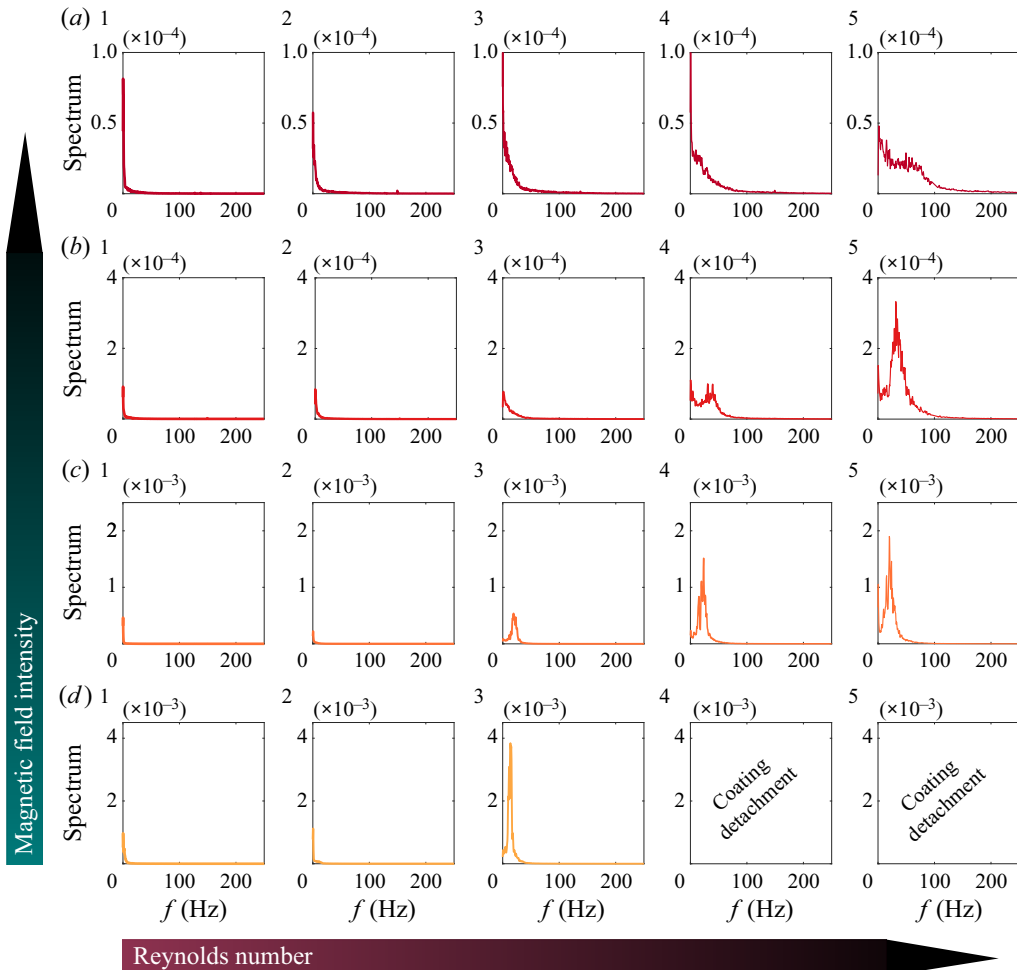


Figure 4. Temporal power spectra of the interface elevation  $\zeta$ . The rows correspond to different magnetic field intensities, while the columns from left to right correspond to increasing Reynolds numbers.

intensities are high, as depicted in the panels of [figure 5\(a.1,a.2\)](#) and [\(b.1,b.2\)](#). However, as the Reynolds number increases and the magnetic field intensity decreases, clear wave crest–trough patterns become evident.

Additionally, in scenarios featuring intermediate Reynolds numbers and higher magnetic field strengths, exemplified by [figure 5](#), e.g. panel [\(a.3\)](#), the interface maintains a relatively flat profile. In contrast, when considering the same Reynolds number but with lower magnetic field intensity, as exemplified in [figure 5\(d.3\)](#), significantly elevated interface profiles become apparent. It is worth noting that for flow cases displaying distinct peaks in the power spectrum diagrams (e.g. [figures 4c.4,c.5](#) or [4d.3](#)), [figure 5](#) shows a regular wave train (monochromatic waves). In cases dominated by a spectrum of frequencies, as seen in [figure 4\(a.5\)](#) numerous harmonics emerge (colours alternate irregularly without a discernible trend) in the space–time diagrams. This observation corroborates our findings from the Fourier space analysis. Furthermore, it is important to highlight that these observations align well with the theoretical predictions shown in [figure 3](#).

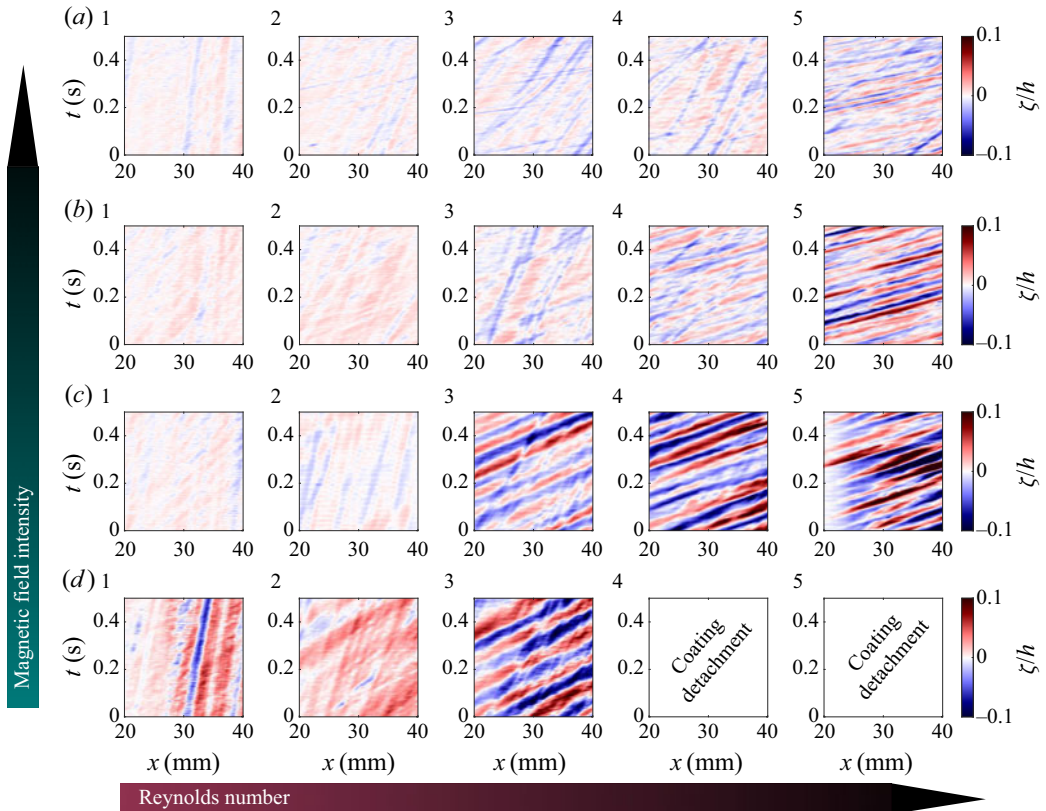


Figure 5. Space–time diagrams of the interface elevation  $\zeta$  for the same experiments shown in figure 4.

### 3.2. Impact of ferrofluid interface stability on the flow

To correlate our observations regarding the characterization of the interface (§ 3.1) with drag reduction, we employ the velocity measurements obtained from 2D-PTV. For clarity, we focus on three distinct flow cases, namely a.5, b.5 and c.5 detailed in table 1, which correspond to the scenarios with the highest Reynolds number ( $Re \approx 12\,500$ ) under varying magnetic field intensities:  $H = 460$  Gs,  $H = 250$  Gs and  $H = 170$  Gs.

In the subsequent part of this section, we normalize the vertical coordinate ( $y$ ) using the channel fluid height ( $D - h$ ) and mirror the bottom half of the velocity profiles, which is bounded by the uncoated wall (figures 6–8, black lines), to ease the comparison with the upper half, which is bounded by the coated wall (figures 6–8, coloured lines). As a result, the origin  $y = 0$  corresponds to both the ferrofluid interface (figures 6–8, coloured lines) and the rigid-wall location (figures 6–8, black lines).

Figure 6(a–c) illustrates the mean streamwise velocity profiles. We note a distinct slip velocity  $U_{slip}$  at the ferrofluid interface for all three experiments, contrasting with the classical no-slip condition observed at the rigid wall. This slip condition at the interface, in conjunction with the zero net mass flow of the ferrofluid (§ 2.2), implies a recirculation within the ferrofluid layer, as shown in Stancanelli *et al.* (2024) and illustrated schematically in figure 1. We also note differences away from the origin implying an asymmetry of the velocity profile in the bulk. While for the strongest magnetic field (figure 6a) the average velocity is always higher on the coated side with respect to the

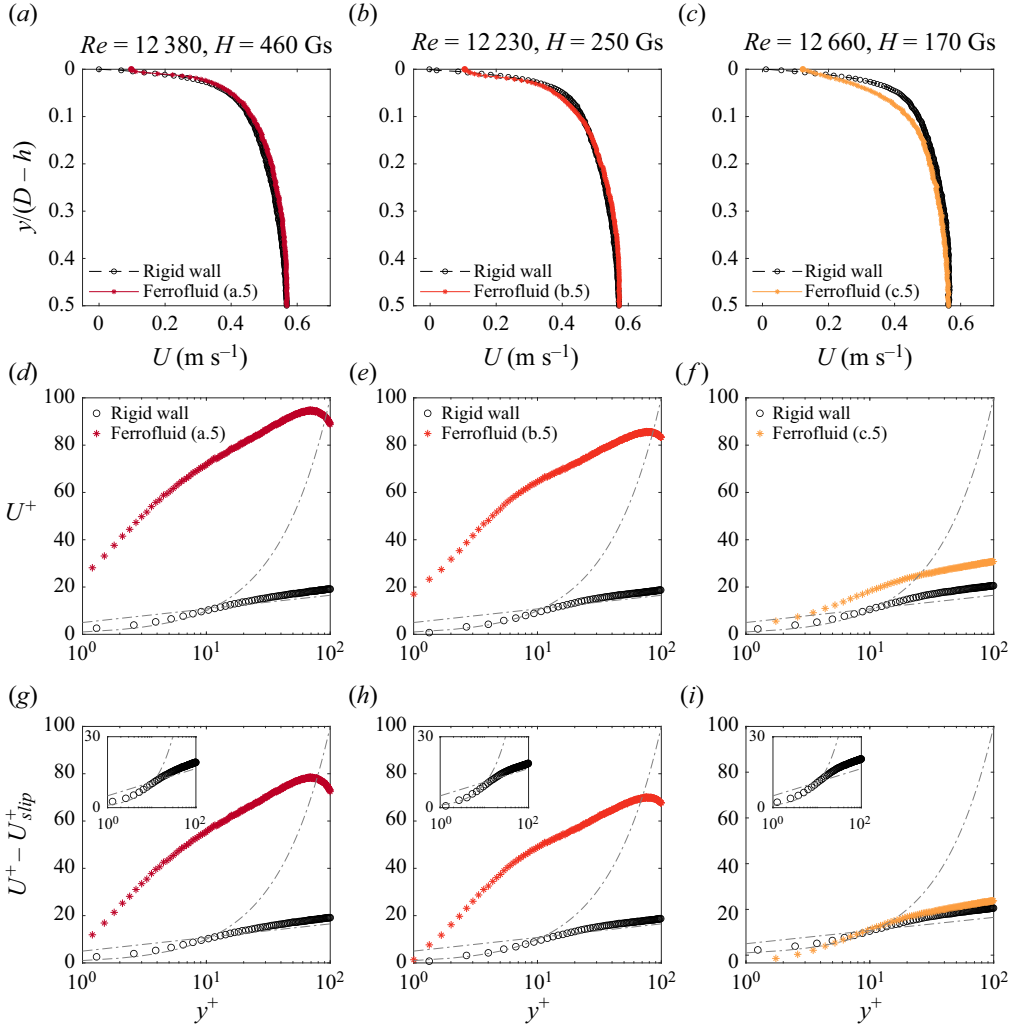


Figure 6. Mean streamwise velocity profiles of a.5, b.5 and c.5 (columns) in large scale units (a–c), wall units (d–f) and wall units with the slip velocity subtracted (g–i). For the colour of the lines see [table 1](#). The corresponding rigid-wall profiles are in black. Inset (g–i): zoom of the rigid wall.

rigid-wall side, for the lowest magnetic field intensity experiments ([figure 6c](#)) the flow is generally faster in the lower half of the channel. In the case of  $H = 250$  Gs the ‘no-slip’ flow is locally faster at  $y/(D-h) \approx 0.05$ . This difference in velocity profiles might be associated with a difference of turbulence intensity in the interface proximity (see below).

[Figure 6\(d–f\)](#) shows the average velocity profiles in wall units  $y^+ = yu_\tau/\nu$  and  $U^+ = U/u_\tau$ , with  $u_\tau = (\tau_0/\rho)^{1/2}$  where  $\tau_0$  is the space and time averaged wall shear stress. For the rigid-wall side, the wall shear stress is  $\tau_0 = \tau_w = \mu \, dU/dy|_{wall}$  evaluated at the wall location, while for the coated wall  $\tau_0$  is evaluated as the total shear stress  $\tau_0 = \tau_c = \mu \, dU/dy - \rho \langle u'v' \rangle$  at the interface location, where  $\rho$  is the water density,  $u'$  and  $v'$  velocity fluctuations in the streamwise and wall-normal directions. Here,  $\langle \cdot \rangle$  denotes averaging over time and the streamwise direction  $x$ , given the statistical stationarity and homogeneity of the flow in  $x$ . Also depicted in [figure 6](#) is the theoretical law of the

wall, comprising the linear law  $u^+ = y^+$  of the viscous sublayer and the logarithmic law  $u^+ = 1/\kappa \ln(y^+) + C^+$  characterizing the log-law region (with  $\kappa = 0.4$  and  $C^+ = 5$ ). As is evident from figure 6(d–f), rigid-wall profile cases are in good agreement with both laws (see also inset in figure 6g–i). Although the presence of the ferrofluid layer makes the velocity profile slightly asymmetric in the bulk (figure 6a–c), this asymmetry is not noticeable in the near-wall region. For the coated-wall profiles, a markedly distinct behaviour is observed. In experiments a.5 and b.5 (figure 6d,e), there is a significant deviation between the experimental velocity profiles and the law of the wall, occurring in both the viscous sublayer and the log-region. In contrast, experiment c.5 (figure 6f) is closer to the no-slip profile. Generally, an upward shift in the velocity profile indicates drag reduction. As reported in Stancanelli *et al.* (2024) concerning an undulating wall with slip velocity, the departure from the law of the wall within the viscous sublayer primarily results from the slip, while the deviation in the log-layer ( $y^+ > 30$ ) is linked to interface waviness. To disentangle the two contributions, in figure 6(g–i), we present the same average velocity profiles in wall units after subtracting the contribution of the slip velocity, denoted as  $U_{slip}$ . A significant difference persists for flow cases a.5 and b.5 (figure 6g,h), particularly evident for  $y^+ > 30$ , whereas the profile of case c.5 nearly conforms to the no-slip profile (figure 6i). This implies that a significant part of the deviation for the c.5 case can be attributed to the slip velocity, while for the other two cases, the primary influence stems from interface waviness.

From figure 6(a–c), we noted that the ferrofluid layer introduces a slip condition at the upper wall of the channel, affecting the shear rate in the channel flow. In figure 7, we further explore the influence of the ferrofluid layer on both viscous and turbulent shear rate profiles. In figure 7(a–c), we present the profiles of the viscous shear rate  $\mu dU/dy$ , where  $\mu$  is the dynamic viscosity of the water and  $U$  the space ( $x$  direction) and time average velocity profile. As expected, the profiles for the rigid wall exhibit a peak precisely at the wall location. Conversely, a distinct behaviour is observed for the coated wall. Close to the interface (at approximately  $y/(D - h) = 0.02$ ),  $\mu dU/dy$  reaches its maximum value, and notably decreases as it approaches the interface due to the slip condition, resulting in a significantly lower value at the interface. This reduction is connected to the change in the gradient of the velocity profile as observed in figure 6, which may be associated with the presence of waves with a moderate amplitude, inducing higher turbulent stresses near the interface as compared with stronger magnetic field cases.

In figure 7(d–f), we present the profiles of the turbulent shear stress  $-\rho\langle u'v' \rangle$ . It is evident that, in the case of the most intense magnetic fields (d–f), the turbulent shear stress is comparable to that observed on the rigid-wall side. In contrast, for lower magnetic intensities,  $-\rho\langle u'v' \rangle$  is higher especially around the peak location  $y/(D - h) \approx 0.08$ . This implies that additional velocity fluctuations are caused by waves, which were observed to have a higher amplitude  $a$  (at  $Re \approx \text{const.}$ ) for lower magnetic fields (§ 3.1).

In figure 7(g–i), we present the Reynolds shear stresses in wall units. Remarkably, for cases with the most intense magnetic field, the peak is closer to the coated wall as compared with the rigid wall (figure 7g–h). A different behaviour is evident in cases of lower magnetic field (figure 7i), where the peak of  $-\rho\langle u'v' \rangle$  aligns with the rigid-wall case. Interestingly, in this case,  $-\rho\langle u'v' \rangle$  remains high and positive in the bulk. This sustained non-zero  $-\rho\langle u'v' \rangle$  value evidences a detrimental impact of the interface instability, i.e. interface waviness causes an additional turbulent shear stress in close proximity to the coated wall.

To further characterize turbulence, in figure 8(a–c), we depict the profile of turbulent kinetic energy ( $tke = \langle u'^2 + v'^2 \rangle$ ). Note that the full  $tke$  also entails  $w'^2$  ( $w'$  is the

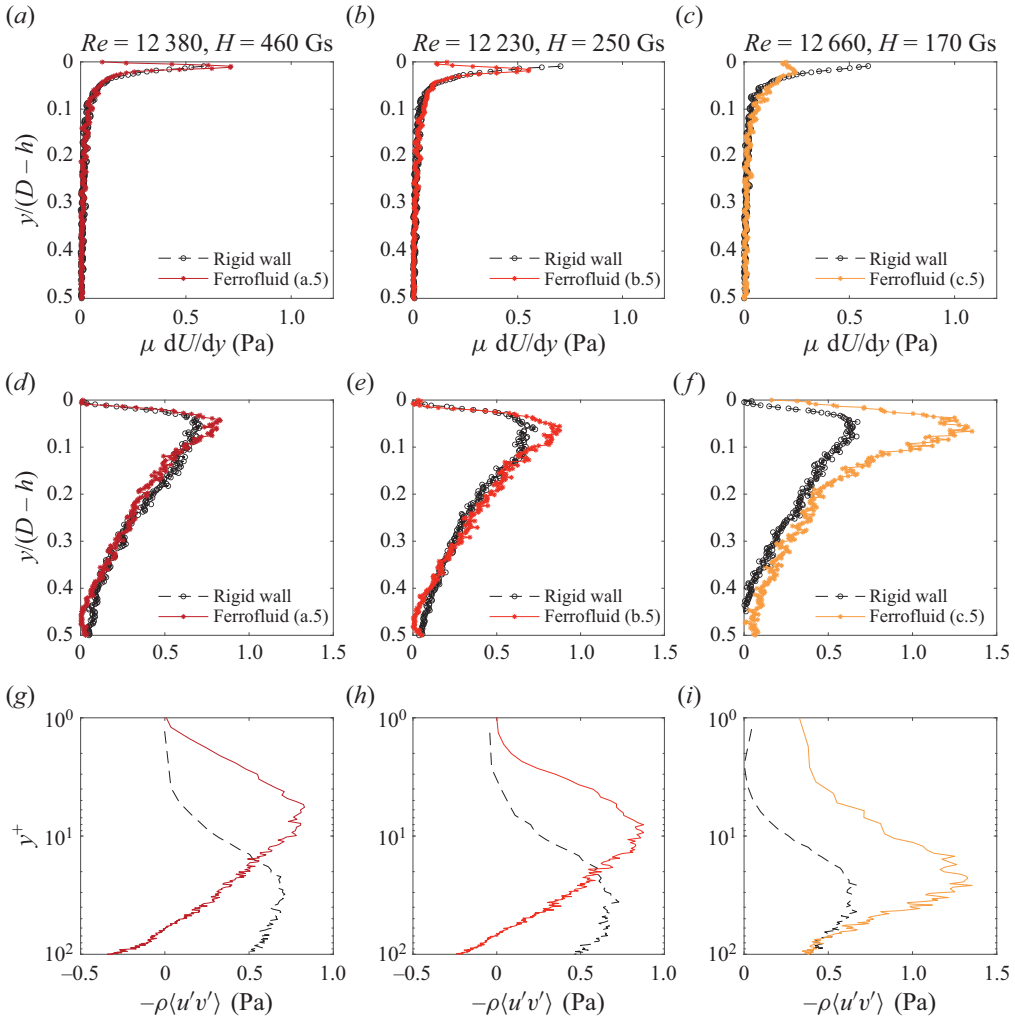


Figure 7. Mean shear rate profiles (a–c) of a.5, b.5 and c.5 (columns) experiments, mean Reynolds shear stress profiles (d–f) and mean Reynolds shear stress profiles in wall units (g–i). For the colour of the lines see [table 1](#). The corresponding rigid-wall profiles are in black.

velocity fluctuation in the span-wise direction), which, however, was not accessible in our measurements. Notably,  $\overline{ike}$  tends to be smaller in flow cases with higher  $H$  ([figure 8a,b](#)) as compared with rigid-wall side, while higher values can be observed for lower magnetic field intensity ([figure 8c](#)). To analyse the individual components, we present in [figure 8\(d–i\)](#) the contributions of the streamwise and wall-normal components. The presence of the coating consistently diminishes the peak value of the streamwise component. However, in the case of lower magnetic field intensity, the wall-normal component experiences a significant increase. This is consistent with the increase in wave amplitude with decreasing  $H$ , as qualitatively noted in [figure 5](#). In essence, the coating proves instrumental in reducing turbulent kinetic intensity up to a point where the waves generated at the interface reach an amplitude substantial enough to markedly elevate the wall-normal velocity fluctuation components.

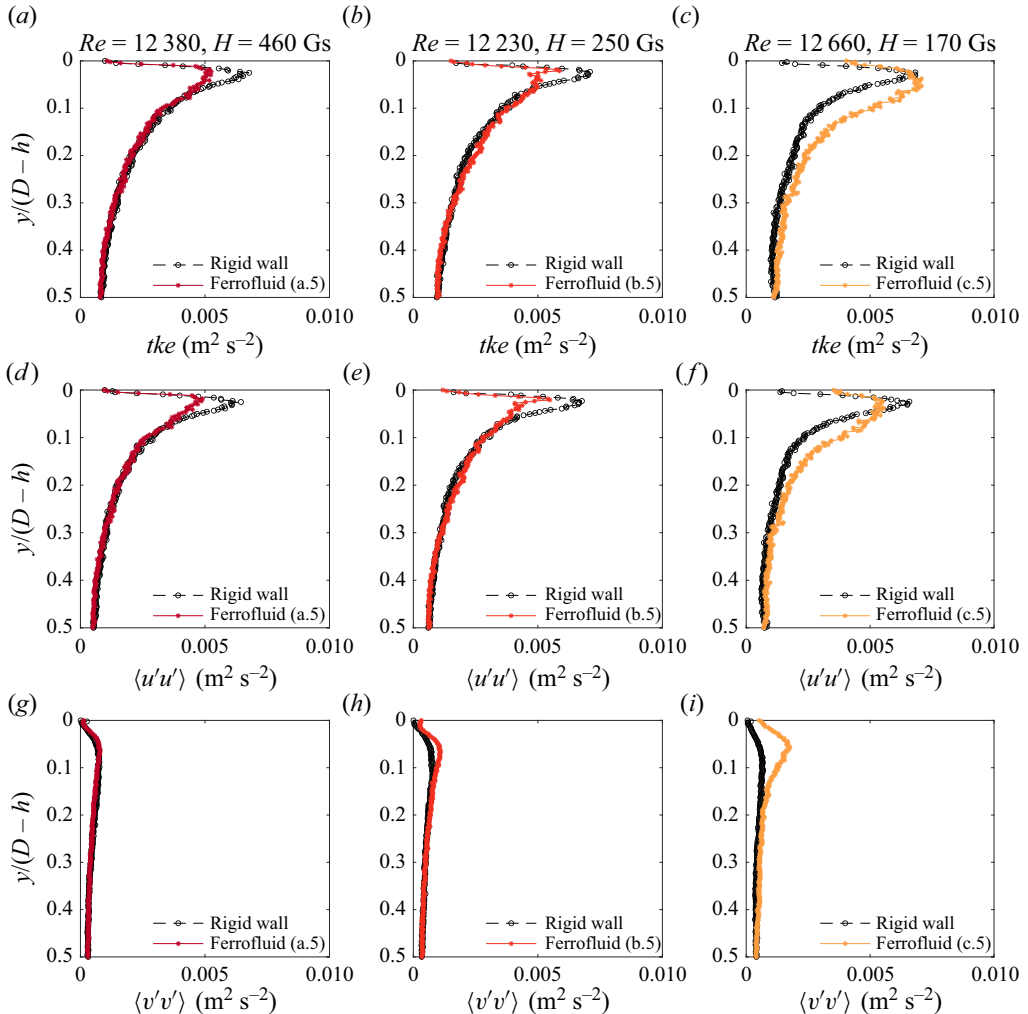


Figure 8. Turbulent kinetic energy profiles (a–c) of a.5, b.5 and c.5 experiments (columns), streamwise velocity (d–f) and wall-normal (g–i) component contribution. For the colour of the lines see [table 1](#). The corresponding rigid-wall profiles are in black.

### 3.3. Drag reduction efficiency in relation to ferrofluid interface stability

We calculate the Fanning friction factor, denoted as  $f = 2\tau_0/(\rho_w U^2)$ , for both the bottom rigid wall and the interface, where  $\rho_w$  is the water density. These results are illustrated in [figure 9\(a\)](#). The figure also includes the theoretical solutions for laminar flow, represented by  $f = c/Re$  with  $c = 14.2$  (Hartnett, Kwack & Rao 1986; Kakaç, Shah & Aung 1987), and turbulent flows, depicted as  $f = 0.079(c_d \cdot Re)^{-1/4}$  with  $c_d = 1.125$  (Jones 1976; Choi & Cho 1999). The figure incorporates friction factor data (depicted in grey) from Stancanelli *et al.* (2024) in which the authors used a similar set-up to the present one. In those experiments, the channel had smaller dimensions, measuring  $10 \times 10$  mm<sup>2</sup> in cross-section, while an array of magnets directly affixed to the upper wall of the channel generated a magnetic field intensity of approximately  $H = 90$  Gs at the ferrofluid interface. Their experimental conditions encompassed both stable and unstable ferrofluid



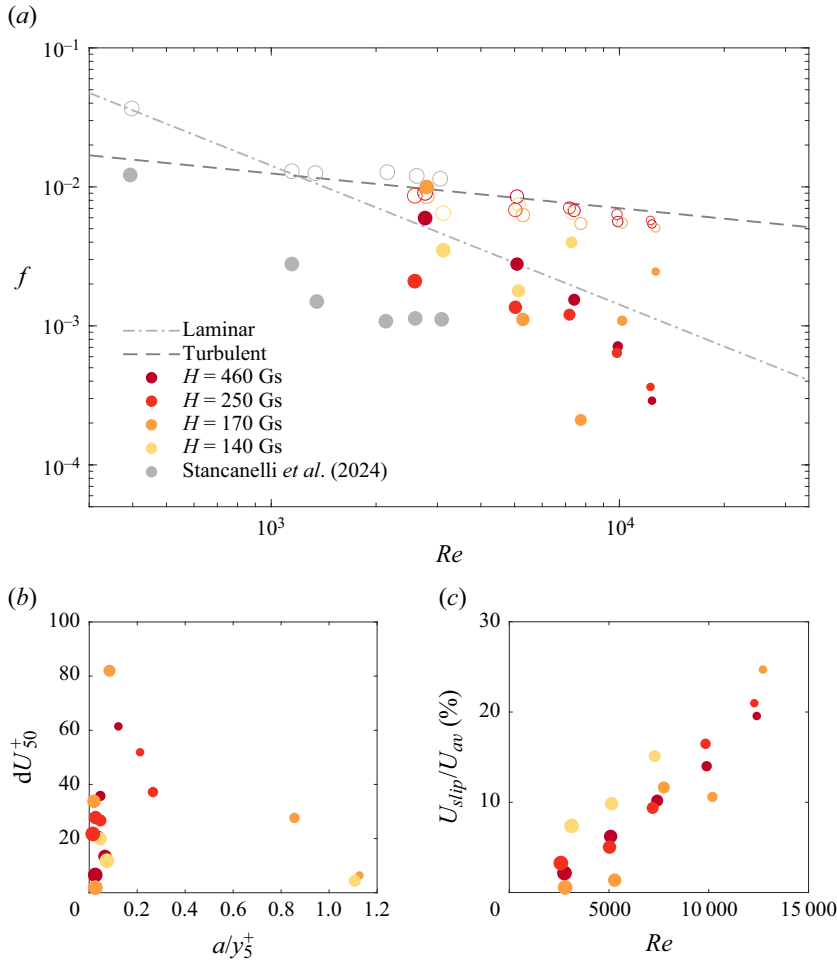


Figure 9. (a) Friction factor  $f$  against the Reynolds number  $Re$ . The filled and the open symbols represent, respectively, the results for the top and the bottom of the channel. For the colours of the symbols, refer to table 1. Grey symbols represent data from Stancanelli *et al.* (2024). Dash-dotted line the solution for turbulent flows, while the dashed line is the solution for laminar flows. (b) Difference between the experimental velocity profile and the theoretical log-law  $dU_{50}^+$  at  $y^+ = 50$ , plotted against the normalized wave amplitude  $a$  with respect to the viscous length scale  $y_5^+$ . (c) Ratio between the slip velocity  $U_{slip}$  and the bulk average velocity  $U_{av}$  against the Reynolds number  $Re$ .

interface scenarios. However, due to the smaller cross-section in their set-up, instability in the ferrofluid interface occurred at relatively low  $Re$  numbers ( $Re < 4000$ ) compared with our current configuration, given the significantly higher bulk average velocity  $U$  at the same  $Re$ .

From figure 9(a), it is evident that the friction factor values for the bottom wall (open symbols) align closely with the turbulent curve. In contrast, the majority of the values at the top interface are significantly below the turbulent curve, in some cases even below the laminar curve. That is, the drag experienced at the interface between the water and ferrofluid is generally much lower compared with that at the bottom of the channel.

Upon closer examination of the coated-wall cases, figure 9(a) illustrates a consistent trend where the friction factor decreases with increasing Reynolds number ( $Re$ ),

particularly evident in experiments conducted with higher magnetic field intensities, namely  $H = 460$  Gs and  $H = 250$  Gs. This holds true also for experiments with lower magnetic field intensities ( $H = 170$  Gs and  $H = 140$  Gs), except for cases at higher Reynolds number where an inversion in this trend occurs (refer to experiments c.4, c.5, and d.3). In these cases, the friction factor increases with  $Re$  at a given  $H$ , albeit remaining below the values observed for a rigid wall. A noteworthy characteristic of experiments c.4, c.5 and d.3 is the high wave amplitudes formed at the interface of the ferrofluid layer compared with other experiments (refer to [figure 5](#)). This may be linked to an increase of the turbulence intensity in the interface proximity due to additional velocity fluctuations connected to the interface instability. Generally, both the slip condition and interface waves contribute to drag reduction. However, when the waves reach high amplitudes, they appear to transition from being advantageous to becoming detrimental. This notion gains additional support through a direct comparison of our experimental data with those presented by Stancanelli *et al.* (2024) (depicted as grey symbols in [figure 9a](#)). Although there is a general consistency in trends between the two datasets, Stancanelli *et al.* (2024) noted smaller friction factors at smaller Reynolds numbers ( $2000 < Re < 4000$ ). This difference could stem from the noted earlier instability of the interface at these Reynolds numbers in their experiments, which augmented drag reduction. In contrast, in the current scenario, the interface remains flat at these Reynolds numbers, with the sole contributing factor being the slip condition.

To analyse a possible relationship between drag reduction and the kinematics of the interface, we illustrate in [figure 9\(b\)](#) the disparity between the experimental velocity profile with subtracted slip velocity (see e.g. [figure 6g–i](#)) and the log-law  $dU_{50}^+$  at  $y^+ = 50$ , plotted against the wave amplitude  $a$  normalized by a viscous length scale, namely 5 wall units ( $y_5^+$ ). The choice of this viscous length scale is motivated by the fact that the viscous shear stress dominates near the ferrofluid interface (see e.g. [figures 8a,b](#) and [8d,e](#)), i.e. even though there is a slip condition there is a viscous layer at the interface in analogy to the viscous sublayer near the solid wall. In [figure 9\(b\)](#),  $dU_{50}^+$  quantifies the effect of the wall waviness on the shear stress. That is, high positive values indicate a lower shear stress at the interface location, signifying drag reduction. Across all experiments, an increase in wave amplitudes corresponds to an increase in  $dU_{50}^+$  as long as  $a$  remains small compared with the viscous length scale. However, when the wave amplitudes approach the viscous length scale (experiments c.4, c.5 and d.3), the advantage derived from surface waviness diminishes significantly. This observation further substantiates our hypothesis that the positive effect of the waves on drag reduction diminishes with wave amplitude and may even become detrimental.

Finally, to complete our analysis of the observed frictional behaviour at the coated wall, we present in [figure 9\(c\)](#) the percentage of slip velocity ( $U_{slip}$ ) relative to the average bulk velocity ( $U_{av}$ ). Notably,  $U_{slip}/U_{av}$  exhibits nearly linear growth with increasing Reynolds numbers in the range covered by our experiments. This is consistent with the Reynolds number trend observed in the friction factor ([figure 9a](#)), where, in general, there is a decrease in  $f$  with  $Re$ , except for cases c.4, c.5 and d.3. Nonetheless, these latter cases are characterized by an elevated slip velocity ([figure 9c](#)), mitigating to some degree the effects of extra velocity fluctuations brought about by the ferrofluid interface waves.

A final element in assessing the effectiveness of the drag reduction technique is the so-called drag reduction coefficient. In [figure 10](#), this coefficient, expressed as  $DR(\%) = (\tau_w - \tau_c)/\tau_w \cdot 100$ , is depicted against the Reynolds number  $Re$ , with  $\tau_w$  denoting the wall shear stress at the rigid wall and  $\tau_c$  representing the corresponding value at the ferrofluid interface. It is evident that, in general, drag reduction tends to increase with the Reynolds

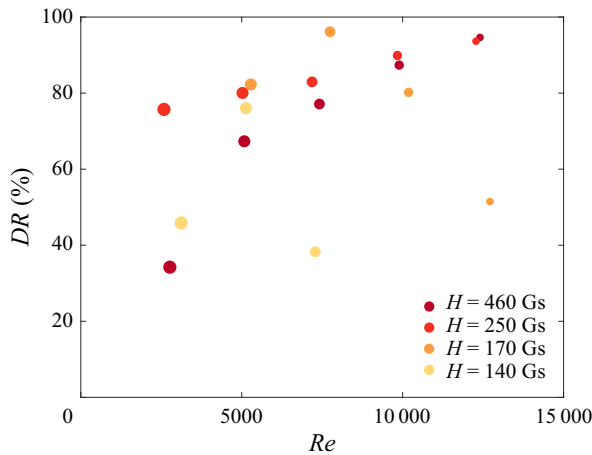


Figure 10. Drag reduction  $DR(\%)$  against the Reynolds number  $Re$ . The colour-coding and symbol size are as specified in table 1. Not shown in the figure, experiment c.1 in which the drag coefficient is slightly negative (drag increase).

number for a given  $H$ , except in cases where the interface wave amplitude is particularly elevated compared with the viscous length scale  $y_5^+$  (flow cases c.4, c.5 and c.5). It is, however, noteworthy that remarkably high values of  $DR$ , up to 95 %, can be achieved, exemplified in scenarios characterized by  $Re \approx 12\,500$  and  $H = 460$  or  $H = 250$ .

#### 4. Conclusions and summary

This study addresses the application of a ferrofluid layer coating to reduce drag in turbulent channel flow with focus on the effect of ferrofluid interface stability. The ferrofluid layer is held in position by permanent magnets, creating a magnetic field oriented tangentially to the interface between the magnetic and diamagnetic fluids. To realize the channel flow a new experimental set-up was devised, while a 2D-PTV and interface identification techniques were employed to capture the flow field and accurately locate the ferrofluid interface.

Firstly, a stability analysis reveals that in experiments with higher flow rates, the interface between the ferrofluid layer and water experiences instability. This instability is confirmed by both a power spectral analysis and height–time diagrams. It was observed that as the Reynolds number increases or the magnetic field intensity decreases, instabilities occur, characterized by the formation of travelling waves on the interface. The amplitude of these waves increases with increasing  $Re$  or decreasing  $H$ . These findings are consistent with the stability theory, further supporting the relationship between forcing, magnetic field intensity and interface stability.

Subsequently, the ferrofluid layer effect on the velocity profile within the channel is investigated. An evident slip velocity emerges at the interface between the two fluids, introducing an asymmetry of the velocity profile between the coated and rigid-wall sides extending into the bulk of the flow. In experiments with a strong magnetic field, the flow is faster on the coated side compared with the rigid-wall side, while the opposite occurs with a lower magnetic field. We inferred that this may be linked to increased shear stresses due to the increasing Reynolds stress with interface wave amplitude. To assess the individual contributions of slip and waviness to the modification of the velocity profile on the coated side, we scrutinize the velocity profiles in wall units. Our findings reveal that at high  $H$ ,

both slip velocity and wall waviness contribute to reduce wall shear stress, leading to an elevation of the velocity profile. Conversely, at low  $H$ , waviness induces extra turbulence. However, the net effect of the ferrofluid interface is still to reduce drag because of the dominant contribution of the slip velocity.

We explored the impact of the ferrofluid layer on viscous and turbulent shear stresses within the channel. Notably, the viscous stress experiences a significant reduction at the interface compared with its solid-wall counterpart, primarily attributable to the slip condition between the two fluids. Conversely, Reynolds shear stresses are elevated in the vicinity of the interface compared with the solid wall, yet they strongly decrease without vanishing at the interface location.

The picture emerging from these observations is as follows: turbulent shear stresses increase near the interface compared with the solid wall when the interface becomes unstable, generating travelling wave patterns. However, right at the interface location, turbulent shear stresses are suppressed due to the non-penetrative condition between the two fluids. Despite the shear stress at the ferrofluid location having an additional turbulent contribution compared with the solid wall, this augmentation does not out-compete the decrease of viscous shear stress due to slip, preserving a lower total shear stress for the coated wall compared with the rigid boundary. As the magnetic field intensity decreases, the Reynolds shear stresses are observed to increase, consistent with the increased turbulence intensity due to larger interface wave amplitudes in this scenario. An analysis of turbulence intensity corroborates this observation, highlighting that the primary contributor to the increase in turbulence intensity with decreasing  $H$  is the augmentation in vertical velocity fluctuations.

The impact of the ferrofluid coating on drag reduction is assessed by examining the friction factor. The results demonstrate that, for most of the flow conditions investigated in this study, the friction factor at the ferrofluid interface is significantly lower compared with the solid wall. Interestingly, this reduction in friction factor persists even when the interface between the two fluids experiences instability, leading to the formation of travelling waves. However, the amplitude of these waves is key in determining whether wall waviness positively or negatively affects drag. Specifically, when the wave amplitude is significantly smaller than the viscous length scale, it has a favourable effect on drag reduction. Conversely, when the amplitude becomes comparable to the viscous length, it becomes detrimental.

**Supplementary movies.** Supplementary movies are available at <https://doi.org/10.1017/jfm.2024.735>.

**Acknowledgements.** We are grateful for financial support from SNSF grant number 200727.

**Declaration of interests.** The authors report no conflict of interest.

#### Author ORCIDs.

✉ Marius M. Neamtu-Halic <https://orcid.org/0000-0002-6438-7967>;

✉ Markus Holzner <https://orcid.org/0000-0003-2702-8612>;

✉ Laura M. Stancanelli <https://orcid.org/0000-0001-9725-9964>.

#### REFERENCES

- CHOI, H., MOIN, P. & KIM, J. 1993 Direct numerical simulation of turbulent flow over riblets. *J. Fluid Mech.* **255**, 503–539.
- CHOI, M. & CHO, K. 1999 Thermal characteristics of a multichip module using PF-5060 and water. *KSME Intl J.* **13**, 443–450.
- COSTANTINI, R., MOLLICONE, J.P. & BATTISTA, F. 2018 Drag reduction induced by superhydrophobic surfaces in turbulent pipe flow. *Phys. Fluids* **30** (2), 025102.

- DEAN, B. & BHUSHAN, B. 2010 Shark-skin surfaces for fluid-drag reduction in turbulent flow: a review. *Phil. Trans. R. Soc. A* **368** (1929), 4775–4806.
- DEV, A.A., DUNNE, P., HERMANS, T.M. & DOUDIN, B. 2022 Fluid drag reduction by magnetic confinement. *Langmuir* **38** (2), 719–726.
- FUKAGATA, K., IWAMOTO, K. & HASEGAWA, Y. 2024 Turbulent drag reduction by streamwise traveling waves of wall-normal forcing. *Annu. Rev. Fluid Mech.* **56**, 69–90.
- GAD-EL HAK, M. 1996 Modern developments in flow control. *Appl. Mech. Rev.* **49**, 365–379.
- HARTNETT, J.P., KWACK, E.Y. & RAO, B.K. 1986 Hydrodynamic behavior of non-Newtonian fluids in a square duct. *J. Rheol.* **30** (4), S45–S59.
- JONES, O.C. JR. 1976 An improvement in the calculation of turbulent friction in rectangular ducts. *Trans. ASME J. Fluids Engng* **98**, 173–180.
- KAKAÇ, S., SHAH, R.K. & AUNG, W. 1987 Handbook of single-phase convective heat transfer. Wiley.
- KIM, J. & HUSSAIN, F. 1993 Propagation velocity of perturbations in turbulent channel flow. *Phys. Fluids A* **5** (3), 695–706.
- KIM, S.J., KIM, H.N., LEE, S.J. & SUNG, H.J. 2020 A lubricant-infused slip surface for drag reduction. *Phys. Fluids* **32** (9), 091901.
- KÖGEL, A., VÖLKE, A. & RICHTER, R. 2020 Calming the waves, not the storm: measuring the Kelvin–Helmholtz instability in a tangential magnetic field. *J. Fluid Mech.* **903**, A47.
- LIRAVI, M., PAKZAD, H., MOOSAVI, A. & NOURI-BORUJERDI, A. 2020 A comprehensive review on recent advances in superhydrophobic surfaces and their applications for drag reduction. *Prog. Organic Coatings* **140**, 105537.
- LUMLEY, J.L. 1969 Drag reduction by additives. *Annu. Rev. Fluid Mech.* **1** (1), 367–384.
- MOLLICONE, J.P., BATTISTA, F., GUALTIERI, P. & CASCIOLA, C.M. 2022 Superhydrophobic surfaces to reduce form drag in turbulent separated flows. *AIP Adv.* **12** (7), 075003.
- NABAE, Y., KAWAI, K. & FUKAGATA, K. 2020 Prediction of drag reduction effect by streamwise traveling wave-like wall deformation in turbulent channel flow at practically high Reynolds numbers. *Intl J. Heat Fluid Flow* **82**, 108550.
- NAKANISHI, R., MAMORI, H. & FUKAGATA, K. 2012 Relaminarization of turbulent channel flow using traveling wave-like wall deformation. *Intl J. Heat Fluid Flow* **35**, 152–159.
- QUADRIO, M. & RICCO, P. 2004 Critical assessment of turbulent drag reduction through spanwise wall oscillations. *J. Fluid Mech.* **521**, 251–271.
- QUADRIO, M., RICCO, P. & VIOTTI, C. 2009 Streamwise-travelling waves of spanwise wall velocity for turbulent drag reduction. *J. Fluid Mech.* **627**, 161–178.
- RICCO, P., SKOTE, M. & LESCHZNER, M.A. 2021 A review of turbulent skin-friction drag reduction by near-wall transverse forcing. *Prog. Aerosp. Sci.* **123**, 100713.
- SARANADHI, D., CHEN, D., KLEINGARTNER, J.A., SRINIVASAN, S., COHEN, R.E & MCKINLEY, G.H. 2016 Sustained drag reduction in a turbulent flow using a low-temperature leidenfrost surface. *Sci. Adv.* **2** (10), e1600686.
- SOLOMON, B.R., KHALIL, K.S. & VARANASI, K.K. 2014 Drag reduction using lubricant-impregnated surfaces in viscous laminar flow. *Langmuir* **30** (36), 10970–10976.
- STANCANELLI, L.M., SECCHI, E. & HOLZNER, M. 2024 Magnetic fluid film enables almost complete drag reduction across laminar and turbulent flow regimes. *Commun. Phys.* **7** (1), 30.
- VIRK, P.S., MICKLEY, H.S. & SMITH, K.A. 1970 The ultimate asymptote and mean flow structure in Toms’ phenomenon. *J. Appl. Mech.* **37**, 488–493.
- VÖLKE, A., KÖGEL, A. & RICHTER, R. 2020 Measuring the Kelvin–Helmholtz instability, stabilized by a tangential magnetic field. *J. Magn. Magn. Matter* **505**, 166693.
- WHITE, C.M. & MUNGAL, M.G. 2008 Mechanics and prediction of turbulent drag reduction with polymer additives. *Annu. Rev. Fluid Mech.* **40**, 235–256.
- ZHANG, X., DUAN, X. & MUZYCHKA, Y.S. 2021 Drag reduction by polymers: a brief review of the history, research progress, and prospects. *Intl J. Fluid Mech. Res.* **48** (6), 1–21.